Long-infrared InAs-based quantum cascade lasers operating at 291K (=19m) with metal-metal resonators

D. Chastanet, G. Lollia, A. Bousseksou, M. Bahriz, P. Laffaille, A. N. Baranov, F. Julien, R. Colombelli, and R. Teissier

Citation: Applied Physics Letters **104**, 021106 (2014); doi: 10.1063/1.4861465
View online: http://dx.doi.org/10.1063/1.4861465
View Table of Contents: http://scitation.aip.org/content/aip/journal/apl/104/2?ver=pdfcov
Published by the AIP Publishing

Over **700** papers & presentations on multiphysics simulation

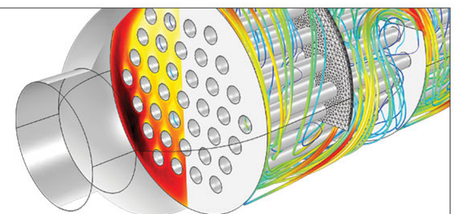

VIEW NOW ▸

This article is copyrighted as indicated in the article. Reuse of AIP content is subject to the terms at: http://scitation.aip.org/termsconditions. Downloaded to IP: 129.175.97.14 On: Wed, 15 Jan 2014 15:12:38

APPLIED PHYSICS LETTERS 104, 021106 (2014)

Long-infrared InAs-based quantum cascade lasers operating at 291 K (λ=19 μm) with metal-metal resonators

D. Chastanet,[1] G. Lollia,[2] A. Bousseksou,[1,a)] M. Bahriz,[2] P. Laffaille,[2] A. N. Baranov,[2] F. Julien,[1] R. Colombelli,[1,b)] and R. Teissier[2,c)]
[1]*Institut d'Electronique Fondamentale, Univ. Paris Sud, UMR 8622 CNRS, 91405 Orsay, France*
[2]*Institut d'Electronique du Sud, Univ. Montpellier 2, UMR 5214 CNRS, 34095 Montpellier, France*

(Received 23 October 2013; accepted 21 December 2013; published online 14 January 2014)

We demonstrate quantum cascade lasers in the InAs/AlSb material system emitting at wavelengths of $\lambda = 19\ \mu$m and $\lambda = 21\ \mu$m. The maximum operating temperatures are 291 K and 250 K, and the threshold current densities at 78 K are as low as 0.6 kA/cm^2 and 1.3 kA/cm^2 for the lasers emitting at $\lambda = 19\ \mu$m and $\lambda = 21\ \mu$m, respectively. These values represent the best performance to date for quantum cascade lasers operating above $\lambda = 16\ \mu$m. Although the devices employ metal-metal waveguide geometries, the diffraction effects which typically hinder the output beam of THz devices are not observed. © *2014 AIP Publishing LLC*. [http://dx.doi.org/10.1063/1.4861465]

The quantum cascade (QC) laser concept is in principle material independent, since its operating principle relies on intersubband unipolar transitions in multiple quantum well (QW) systems:[1] the width of the QW—and not the semiconductor material—sets the emission wavelength. To date, QC lasers (QCLs) have been demonstrated in three major material families: InGaAs/AlInAs on InP substrates; GaAs/AlGaAs on GaAs substrates; and antimonides materials, such as InAs/AlSb on InAs substrates,[5] InGaAs/AlAsSb on InP substrates,[22] or—recently—InGaAs/GaAsSb on InP.[23] As a matter of fact, each of these materials best suits a specific wavelength range, due to differences in electronic effective mass, conduction band offset, and index of refraction.

The material of choice for mid-infrared (IR) applications is InGaAs/AlInAs, with excellent performances demonstrated in the whole mid-IR, from 3.5 μm to 10 μm and beyond.[2] The GaAs/AlGaAs system is the preferred material for THz applications ($65\mu m < \lambda < 250\mu m$). In combination with the metal–metal waveguide geometry,[3] maximum operating temperatures (T_{max}) of almost 200 K have been achieved.[4] InGaAs/GaAsSb on InP is an alternative material for THz QC lasers.[23] Finally, InAs-based QCLs were originally developed for short infrared wavelengths ($\lambda \sim 2.6$–3.5 μm),[5] taking benefit of the large conduction band-offset available.

A main advantage of the InAs/AlSb system is, however, the very low electronic effective mass in the InAs quantum wells ($0.023 \cdot m_0$; m_0 is the electron mass), which provides elevated optical gains. This is especially true at very long-IR wavelengths, where non-parabolicity effects are weak.[6,7] While mid-IR QC lasers are now commercial devices, at longer IR wavelengths little studies have been reported, and the performances are still poor. This region ($19\ \mu m < \lambda < 25\ \mu m$) corresponds to an atmospheric window and it is of special interest—for instance—for applications in astronomical observations. The initial studies which contributed to the emergence of THz QC lasers were carried out from 1998 to 2002,[8–12] with emission wavelengths of InGaAs- and GaAs-based QCLs from 19 μm to 24 μm, and still represent the current state of the art. Recently, however, InAs/AlSb QC lasers emitting at $\lambda \approx 20\ \mu$m have been demonstrated.[13]

In this Letter, we report recent developments on InAs/AlSb based QC lasers operating at wavelengths of 19 μm and 21 μm, with improved design and metal–metal ridge resonators. The T_{max} achieved −291 K at $\lambda = 19\ \mu$m and 250 K at $\lambda = 21\ \mu$m—represent a new state of the art at long IR wavelengths. It is also well known that—for THz QC lasers—the use of metal–metal waveguides is hampered by very diverging far-fields.[14] Here, we show that at these wavelengths these undesirable diffraction effects appear to be absent.

The two active region designs employed in this work are presented in Figure 1. The first design is very similar to the one reported in Ref. 13, but with a modified injector and higher doping of the active region, aiming to increase the current dynamics. It is based on a diagonal intersubband transition in 4 coupled-QWs, with a double phonon extraction, as shown in Fig. 1(a). The nominal transition energy is 62 meV ($\lambda = 20.0\ \mu$m), with a dipolar matrix element (dipole length) of 6.2 nm. A second active region, with a vertical transition (i.e., maximizing the oscillator strength) has been studied. The layer structure is described in Fig. 1(b), taking into account the actual InAs layer thickness given by X-ray diffraction measurements, which proved to be 8% more than the nominal value. The calculated transition energy is 68 meV ($\lambda = 18.2\ \mu$m), with a dipolar matrix element of 8.1 nm. The upper state lifetimes due to LO-phonon scattering are estimated to be 1.2 ps for design 1 and 0.76 ps for design 2 at a temperature of 80 K. The actual lifetimes are also reduced by interface roughness scattering. This is particularly important in this material system, because of the very large conduction band discontinuity $U = 2.1$ eV between InAs and AlSb. We can estimate the strength of this mechanism using the conventional description of the roughness with an average step height Δ and in plane correlation length Λ[15]

a)E-mail: adel.bousseksou@u-psud.fr
b)E-mail: raffaele.colombelli@u-psud.fr
c)E-mail: teissier@univ-montp2.fr

 © 2014 AIP Publishing LLC

This article is copyrighted as indicated in the article. Reuse of AIP content is subject to the terms at: http://scitation.aip.org/termsconditions. Downloaded to IP: 129.175.97.14 On: Wed, 15 Jan 2014 15:12:38

$$\frac{1}{\tau_{ij}^{IFR}} = \frac{\pi m^*}{\hbar^3} \Delta^2 \Lambda^2 e^{-\frac{\Lambda^2 q_{ij}^2}{4}} U^2 \sum_n |\chi_i(x_n)\chi_f(x_n)|^2, \quad (1)$$

where m* is the electron effective mass, q_{ij} the in plane momentum associated to the intersubband scattering from subband i to subband j, and $\chi_i(x_n)$ and $\chi_f(x_n)$ are the amplitude of the initial and final wavefunctions at the interface x_n. The absolute values of these times are difficult to calculate precisely, since they strongly depend on the roughness parameters. With tentative values of $\Delta = 0.08$ nm and $\Lambda = 3$ nm, we obtain an upper level interface scattering time of 0.77 ps for design 1 and 0.34 ps for design 2. The total value of the relevant lifetimes, including phonon scattering and interface roughness, are $\tau_{up} = 0.46$ ps (upper state lifetime), $\tau_{u\text{-}l} = 1.8$ ps (scattering time from upper to lower state), and $\tau_{low} = 0.32$ ps (lower state lifetime) for design 1 and $\tau_{up} = 0.23$ ps, $\tau_{u\text{-}l} = 1.9$ ps, and $\tau_{low} = 0.29$ ps for design 2.

This permits to calculate the theoretical optical gain, with the usual expression for a QC laser[1]

$$g = \frac{4\pi e \langle z_{u-l}\rangle^2}{\varepsilon_0 n \lambda 2\gamma L_p} \eta_i \tau_{up} \left(1 - \frac{\tau_{low}}{\tau_{u-l}}\right), \quad (2)$$

where $z_{u\text{-}l}$ is the dipolar matrix element between the upper and lower laser levels, λ the emission wavelength, 2γ the full width of the radiative transition ($\sim$10% of the transition energy), L_p the length of one period of active region, $n \approx 3.3$ the effective index of the optical mode, and η_i the injection efficiency assumed to be unity. Eq. (2) gives g = 82 cm/kA for design 1 and g = 43 cm/kA for design 2.

We studied two QCL structures based on these two designs. Sample D605 consists of 80 periods of the design 1, while sample D686 consists of 70 periods of design 2. All the samples were grown on an n-InAs substrate, in a Riber Compact 21 solid source molecular beam epitaxy (MBE) reactor. A double etch-stop layer section made of AlAsSb/InAs/AlSb (200/100/5 nm) was grown before the active region to enable the implementation of a metal–metal waveguide geometry.

At these very long IR wavelengths, metal–metal waveguides are advantageous with respect to standard dielectric waveguides,[11] both in terms of figure of merit (defined as Γ/α, with Γ the active region confinement factor, and α the total losses) and of practicality, since the growth of prohibitively thick semiconductor cladding layers is unnecessary. We have employed the same protocol traditionally used for THz QC lasers with metal–metal waveguides:[16] the device fabrication starts with Au–Au thermo-compressive wafer bonding onto an InAs carrier wafer, followed by initial substrate and stop layers removal with citric acid and an HCl-based solution, respectively.

The laser ridges were defined by contact optical lithography followed by wet chemical etch with $H_3PO_4/H_2O_2/H2O$ (2:1:1). In order to obtain almost vertical/in-slanted sidewalls (Fig. 2) and avoid excessive lateral dispersion of the injected current, it is important to align the ridges along the (011) crystal direction. The ridge width must be kept relatively narrow to (i) reduce the total injected power and (ii) guarantee laser operation on the fundamental TM_{00} transverse mode. A judicious choice lies in the 20–30 μm range. However, it prevents direct wire bonding on the ridge top surface; the implementation of deported electrical contacts is thus necessary. An insulation layer (300 nm of Si_3N_4) was deposited by plasma enhanced chemical vapor deposition (PECVD) at 300 °C and then opened on top of the ridges by reactive-ion etching (RIE). Deposition of the top contact (Ti/Au), followed by sample thinning and back-contact deposition concludes the processing. A typical result is shown by the colorized SEM image in Fig. 2.

The optoelectronic characterizations of sample D605 are reported in Fig. 3. The laser operates up to 250 K (Fig. 3(a)) in pulsed mode, with 100 ns current pulses at a repetition rate of 100 kHz. The emission wavelength spans a range from 21.3 μm at low temperature to 20.7 μm at 250 K (Fig. 3(b)). The signal was collected by a f/2 off-axis parabolic mirror

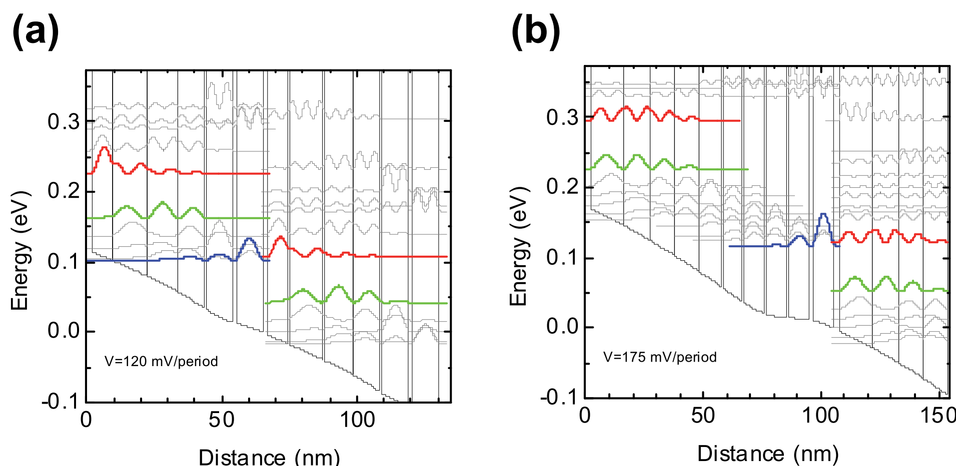

FIG. 1. Conduction band profile of two periods of the studied QCL active regions and moduli squared of the electron wavefunctions. The optical transition involves red (upper) and green (lower) states. (a) One period of design 1 consists of the following layers (in Å and starting from the injection barrier): **20**/73/**3**/127/**2**/108/**2**/100/**7**/98/**12**/100, where AlSb layers are in bold and a Si-doped layer (n = 1.5 × 10^{17} cm^{-3}) is underlined. The nominal emission wavelength is here $\lambda = 20\,\mu$m. (b) One period of design 2 consists of the following layers (in Å and starting from the injection barrier): **21**/139/**1.5**/111/**1.5**/102/**3**/99/**6**/91/**6**/85/**6**/84/**9**/84/**12**/90/**15**/91, where AlSb layers are in bold and the Si-doped layer (n = 1.3 × 10^{17} cm^{-3}) is underlined. The nominal emission wavelength is here $\lambda = 18.2\,\mu$m.

This article is copyrighted as indicated in the article. Reuse of AIP content is subject to the terms at: http://scitation.aip.org/termsconditions. Downloaded to IP: 129.175.97.14 On: Wed, 15 Jan 2014 15:12:38

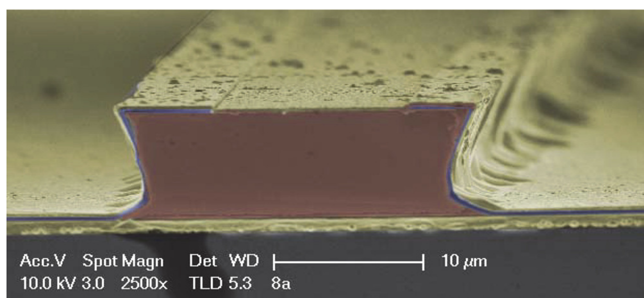

FIG. 2. Colorized SEM image of the cleaved facet view of a typical laser device obtained from sample D686. The red section corresponds to the active region (7 μm thick), the yellow ones to the contact layers (Ti/Au), and the violet section highlights the SiN insulating layer.

and measured with a He-cooled Silicon bolometer. The spectra are obtained with a Fourier transform infrared (FTIR) spectrometer in rapid scan using the same detector. The threshold current density (J_{th}) at 80 K is $\approx$1.3 kAcm^{-2}. It is similar to the one obtained in Ref. 13 for a similar wavelength of $\approx$20 μm. The doping level of sample D605 corresponds to an electron density of 1.5×10^{11} cm^{-2}, 50% larger than the one used in Ref. 13. It is shown here that the increased doping has no negative impact on the laser threshold current, but provides a larger current dynamic ($J_{max} > 4$ kA/cm^2). This, in part, permits to reach a significantly higher operating temperature, better than previously reported values for QC lasers emitting at this wavelength.[10,11]

The best experimental results on sample D686 are reported in Fig. 4. The threshold current density at 78 K exhibits a low value of $\approx$600 Acm^{-2}, and the devices operate in pulsed regime up to 291 K. The laser operating wavelength is $\lambda \approx 19\,\mu$m, as shown by the spectra acquired at different temperatures in Fig. 4(b). Not only 291 K is the highest reported temperature to date for QC lasers operating at this wavelength,[17,18] but the J_{th} at 78 K is about 3 times lower with respect to the previous demonstrations in the InGaAs/AlInAs material system. This reduction is a direct consequence of the very low electronic effective mass of InAs (0.023, instead of 0.047 in InGaAs) and the large resulting optical gain. A rough estimation leads, in fact, to a peak gain approximately 2.6 times higher,[5] in good agreement with the observed J_{th} reduction, assuming everything else is equal.

In both samples, the measured laser emission is slightly shifted towards lower energy as compared to the calculated transition energy, by a value of about 4 meV. It must be pointed out here that the AlSb barrier thicknesses are extremely small in the active region of these QCLs (2 Å in D605 and 1.5 Å in D686). We are confident that we reliably

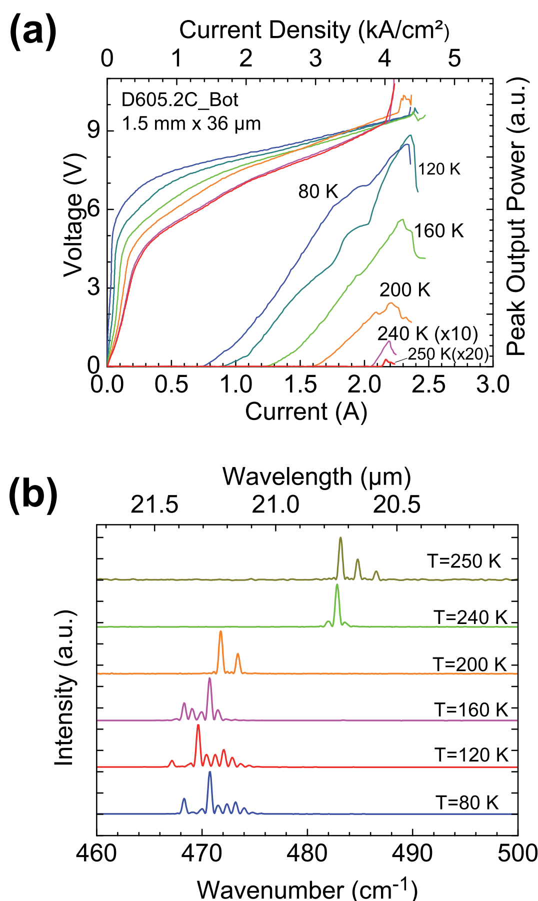

FIG. 3. Experimental results obtained on sample D604 ($\lambda = 21\,\mu$m) under pulsed current injection (100 ns pulses, 100 kHz repetition rate) using a FTIR spectrometer equipped with Silicon bolometer. The laser ridge dimensions are 1.50 mm $\times$ 36 μm. (a) Current-voltage (IV) and light-current (IL) characteristics at different heat-sink temperatures. (b) Emission spectra.

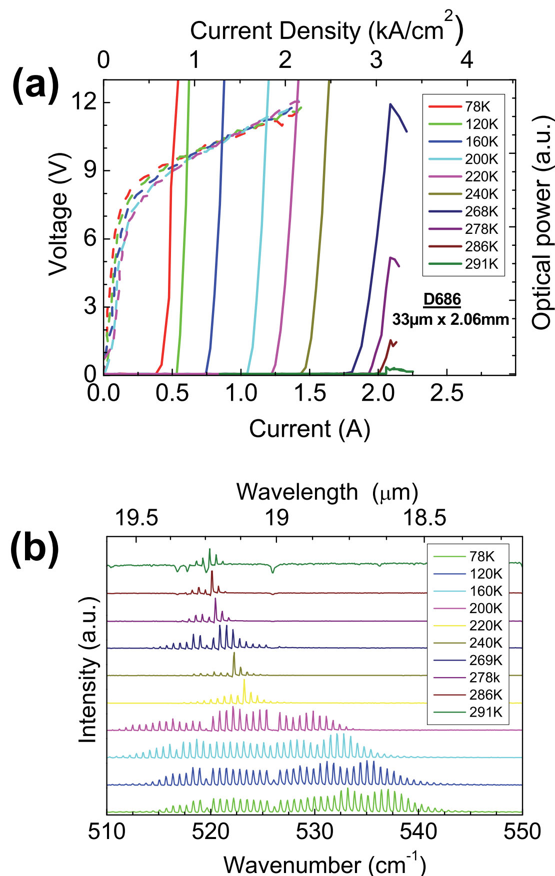

FIG. 4. Experimental results obtained on sample D686 ($\lambda = 19\,\mu$m) under pulsed current injection (50 ns pulses, 84 kHz repetition rate) using a FTIR equipped with an external MCT detector. The laser ridge dimensions are 2.01 mm $\times$ 33 μm. (a) IV and IL characteristics at different heat-sink temperatures. (b) Emission spectra acquired at different heat-sink temperatures above laser threshold.

This article is copyrighted as indicated in the article. Reuse of AIP content is subject to the terms at: http://scitation.aip.org/termsconditions. Downloaded to IP: 129.175.97.14 On: Wed, 15 Jan 2014 15:12:38

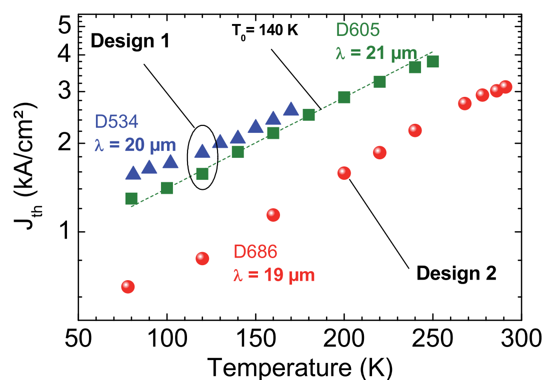

FIG. 5. Threshold current densities (J_{th}) as a function of the heat-sink temperature (T) for the different samples tested: D605 (green squares), D686 (Red dots), and D534 (Blue triangles). The T_0 parameter is estimated according to the formula, $J_{th} = J_0 e^{T/T_0}$.

control the growth of such sub-atomic layers. Nevertheless, the observed energy shift can be explained by a small shift of the effective thicknesses of these AlSb barriers.

Samples D605 ($\lambda = 21\,\mu$m) and D534 of Ref. 13 ($\lambda = 19\,\mu$m) share the same semi-diagonal intersubband transition (design 1), and their J_{th} are consistently a factor of about 2 higher than sample D686 ($\lambda = 19\,\mu$m) based on a vertical transition (design 2), regardless of the exact emission wavelength, as shown in Fig. 5. They all have a similar temperature dependence of the threshold current, with a characteristic temperature T_0 of 140 K. These experimental results demonstrate that the active region based on a spatially direct transition is superior to the semi-diagonal. However, they are in contradiction with the theoretical comparison of the two designs described above. The IV characteristics (Figs. 3(a) and 4(a)) exhibit a similarly sharp turn-on behavior; hence, a strong effect due to non-perfect current injection into the upper laser state can be safely excluded. Also, we can rule out the proximity of the phonon band at $\lambda = 21\,\mu$m given that InAs phonons are located at even lower energies with respect to GaAs or InGaAs.[19] One explanation of this discrepancy could be that the internal losses are dramatically different between samples D534/D605 and sample D686. This would have to be confirmed by waveguide loss measurements, such as cavity length dependence measurements. Another reason could be found in the accuracy of the calculation of interface roughness scattering times. However, even if the roughness parameters Δ and Λ can be questioned, the geometrical part of Eq. (1), which involves the wavefunctions, always leads to a larger scattering rate in design 2 as compared to design 1, in contradiction with the experimental results.

The last point we address is the far-field pattern of the emitted beam. It is well known that—for THz QC lasers—the use of metal–metal waveguides is hampered by very diverging far-fields.[14] This explains why the problem of beam-shaping has received such a large attention.[20] The origin of the problem stems from the large difference between the active region thickness (L) and the emission wavelength (λ). In the THz, the ratio L/λ is typically 0.1 or less: This very low value yields elevated facet reflectivity (≈70%/80%) and heavy diffractive effects.[21] In our case, L/λ is approximately 0.36: on paper, this value yields a facet reflectivity of 35%, i.e., close to the value for a plane wave. We should therefore expect well behaved output beams, despite the fact that a metal–metal waveguide is employed.

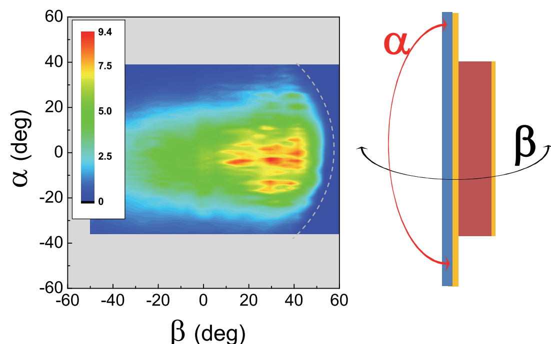

FIG. 6. Experimental far-field emission pattern of the D686 laser device reported in Fig. 2. The measurement is performed at 78 K using a liquid nitrogen cooled MCT detector. The setup maximum angular resolution is ≈0.4°. However, the far-fields have been acquired in steps of 3° along β and 1° along α. The sample is held in a cryostat with a 2-in. diameter ZnSe window. (The dark grey dashed line corresponds to maximum accessible angular range). The diffractive effects typical of metal–metal QC lasers appear to be absent.

Figure 6 reports the experimental far-field emission pattern of the processed device shown in Fig. 2. It is obtained at 78 K with a Mercury–Cadmium–Telluride (MCT) detector (active detector size: 1mm × 1 mm), which was scanned on a 10-cm-radius sphere centered on the device surface. These parameters yield an angular resolution of ≈0.57°. The far-fields have been acquired in steps of 3° along β and 1° along α (see Fig. 6 for angular direction definitions). Diffractive effects appear to be absent, and a single lobed far-field emission with a 40° × 60° divergence is observed instead. Furthermore, the QC laser evidently operates on the TM_{00} mode. The result—which we have reproduced on several devices—suggests that indeed the power extraction from the laser facet can be as efficient as for mid-IR devices. It is a major simplification which strengthens the case in favor of this material system for long IR QC lasers.

In conclusion, we have demonstrated QC lasers emitting at $\lambda = 19\,\mu$m and $\lambda = 21\,\mu$m in the InAs/AlSb material system, with metal–metal waveguides and featuring the highest maximum operating temperatures to date for this wavelength range. The use of metal–metal waveguides does not hamper the quality of the far-field emission patterns. The threshold current densities are about 3 times lower than for similar devices, in the InGaAs/AlInAs or GaAs/AlGaAs material systems, thanks to the low electronic effective mass in the InAs QWs. This result is also extremely promising for the THz range of the electromagnetic spectrum, where InAs-based QC lasers should exhibit extremely low J_{th} with—possibly—improved temperature behavior.

We thank Nathalie Isac for help with the wafer-bonding process. We acknowledge financial support from the French National Research Agency (No. ANR-11-NANO-020 "DELTA") and by the Collaborative Action (No. 8748RA12) between the CEA and the University Paris Sud. The device fabrication has been performed at the nano-center CTU-IEF-Minerve—part of the French RENATECH network—which was partially funded by the Conseil Général de l'Essonne.

This article is copyrighted as indicated in the article. Reuse of AIP content is subject to the terms at: http://scitation.aip.org/termsconditions. Downloaded to IP: 129.175.97.14 On: Wed, 15 Jan 2014 15:12:38

[1] *Intersubband Transitions in Quantum Structures*, edited by R. Paiella (McGraw-Hill, 2006).
[2] Y. Yao, A. J. Hoffman, and C. F. Gmachl, Nat. Photonics **6**, 432–439 (2012), and references therein.
[3] S. Kohen, B. S. Williams, and Q. Hu, J. Appl. Phys. **97**, 053106 (2005).
[4] S. Fathololoumi, E. Dupont, C. W. I. Chan, Z. R. Wasilewski, S. R. Laframboise, D. Ban, A. Mátyás, C. Jirauschek, Q. Hu, and H. C. Liu, Opt. Express **20**, 3866–3876 (2012).
[5] O. Cathabard, R. Teissier, J. Devenson, J. Moreno, and A. N. Baranov, Appl. Phys. Lett. **96**, 141110 (2010).
[6] E. Benveniste, A. Vasanelli, A. Delteil, J. Devenson, R. Teissier, A. Baranov, A. M. Andrews, G. Strasser, I. Sagnes, and C. Sirtori, Appl. Phys. Lett. **93**, 131108 (2008).
[7] M. Helm "The basic physics of intersubband transitions," in *Intersubband Transitions in Quantum Wells: Physics and Device Applications I*, Semiconductors and Semimetals Vol 62, edited by H. C. Liu and F. Capasso (Academic, 2000), Chap. I.
[8] A. Tredicucci, C. Gmachl, F. Capasso, D. L. Sivco, A. L. Hutchinson, and A. Y. Cho, Appl. Phys. Lett. **74**, 638 (1999).
[9] A. Tredicucci, C. Gmachl, M. C. Wanke, F. Capasso, A. L. Hutchinson, D. L. Sivco, S. N. G. Chu, and A. Y. Cho, Appl. Phys. Lett. **77**, 2286 (2000).
[10] R. Colombelli, F. Capasso, C. Gmachl, A. L. Hutchinson, D. L. Sivco, A. Tredicucci, M. C. Wanke, A. M. Sergent, and A. Y. Cho, Appl. Phys. Lett. **78**, 2620 (2001).
[11] K. Unterrainer, R. Colombelli, C. Gmachl, F. Capasso, H. Y. Hwang, A. M. Sergent, D. L. Sivco, and A. Y. Cho, Appl. Phys. Lett. **80**, 3060–3062 (2002).
[12] J. Ulrich, J. Kreuter, W. Schrenk, G. Strasser, and K. Unterrainer, Appl. Phys. Lett. **80**, 3691 (2002).
[13] M. Bahriz, G. Lollia, P. Laffaille, A. N. Baranov, and R. Teissier, Electron. Lett. **49**, 1238 (2013).
[14] E. Orlova, J. N. Hovenier, T. O. Klaassen, I. Kašalynas, A. J. L. Adam, J. R. Gao, T. M. Klapwijk, B. S. Williams, S. Kumar, Q. Hu, and J. L. Reno, Phys. Rev. Lett. **96**, 173904 (2006).
[15] T. Ando, A. B. Fowler, and F. Stern, Rev. Mod. Phys. **54**, 437 (1982).
[16] Y. Chassagneux, J. Palomo, R. Colombelli, S. Dhillon, C. Sirtori, H. Beere, J. Alton, and D. Ritchie, Appl. Phys. Lett. **90**, 091113 (2007).
[17] R. Colombelli, A. Tredicucci, C. Gmachl, F. Capasso, D. L. Sivco, A. M. Sergent, A. L. Hutchinson, and A. Y. Cho, Electron. Lett. **37**, 1023 (2001).
[18] J. A. Fan, M. A. Belkin, M. Troccoli, S. Corzine, D. Bour, G. Höfler, and F. Capasso, Electron. Lett. **43**, 1284 (2007).
[19] E. D. Palik, *Handbook of Optical Constants of Solids* (Academic, 1998).
[20] C. Sirtori, S. Barbieri, and R. Colombelli, Nature Photon. **7**, 691 (2013).
[21] J. A. Encimar and J. M. Rebollar, IEEE Trans. Microwave Theory Tech. **34**, 809–814 (1986).
[22] J. P. Commin, D. G. Revin, S. Y. Zhang, A. B. Krysa, K. Kennedy, and J. W. Cockburn, Appl. Phys. Lett. **97**, 031108 (2010).
[23] C. Deutsch, M. Krall, M. Brandstetter, H. Detz, A. M. Andrews, P. Klang, W. Schrenk, G. Strasser, and K. Unterrainer, Appl. Phys. Lett. **101**, 211117 (2012).

This article is copyrighted as indicated in the article. Reuse of AIP content is subject to the terms at: http://scitation.aip.org/termsconditions. Downloaded to IP: 129.175.97.14 On: Wed, 15 Jan 2014 15:12:38